4

An Ultra-Low Phase Noise Class-F_2 CMOS Oscillator

In this chapter, we discuss and analyze a class of operation of an RF oscillator that further minimizes its phase noise. The main idea is to enforce a clipped voltage waveform around the LC tank by increasing the second harmonic of fundamental oscillation voltage through an additional impedance peak, thus giving rise to a class-F_2 operation. As a result, the noise contribution of the tail current transistor on the total phase noise can be significantly decreased without sacrificing the oscillator's voltage and current efficiencies. Furthermore, its special impulse sensitivity function (ISF) reduces the phase sensitivity to thermal circuit noise. The prototype of the class-F_2 oscillator is implemented in standard TSMC 65 nm CMOS occupying 0.2 mm^2. It draws 32–38 mA from 1.3-V supply. Its tuning range is 19% covering 7.2–8.8 GHz. It exhibits phase noise of -139 dBc/Hz at 3-MHz offset from 8.7-GHz carrier, translated to an average figure of merit of 191 dBc/Hz with less than 2-dB variation across the tuning range.

4.1 Introduction

Spectral purity of RF LC-tank oscillators is typically addressed by improving a quality factor (Q) of its tank, lowering its noise factor (NF) and increasing its power consumption. Even though technology scaling increases the *effective* capacitance ratio, $C_{max}/_{min}$, of switchable tuning capacitors and, consequently, the oscillator tuning range, it does not improve the oscillator's spectral purity parameters, such as tank Q-factor and oscillator NF. In fact, the tank Q-factor is slightly degraded in more advanced technologies mainly due to closer separation between the top metal and lossy substrate as well as

thinner lower-level metals that are used in metal-oxide-metal (MoM) capacitors. On the other hand, transistor noise factor keeps on degrading in more advanced technologies. Consequently, NF increases and thus penalizes the oscillator phase noise (PN). Consequently, the oscillators of excellent spectral purity and power efficiency are becoming more and more challenging as compared to other RF circuitry that is actually gaining from the technology scaling. This has motivated an intensive research leading to new oscillator topologies [1–11].

In this chapter, we specifically address the ultra-low phase noise design space while maintaining high power efficiency. We describe a soft-clipping class-F_2 oscillator topology based on enforcing a clipped voltage waveform around the LC tank by increasing the second-harmonic of the fundamental oscillation voltage through an additional impedance peak [8–10]. This structure shifts the oscillation voltage level so that it provides enough headroom for the tail current without compromising the oscillating amplitude. Consequently, the phase noise contribution of the tail current transistor is effectively reduced while maintaining the oscillator voltage efficiency. Furthermore, the class-F_2 operation clips the oscillation waveform for almost half of the period, thus benefiting from the lower circuit-to-phase-noise conversion during this time span.

The chapter is organized as follows: the trade-offs between the RF oscillator PN and power consumption are investigated in Section 4.2. Section 4.3 establishes the environment to introduce the class-F_2 operation, its benefits, and constraints. The circuit-to-PN conversion mechanisms are studied in Section 4.4. Section 4.5 presents extensive experimental results.

4.2 Challenges in Ultra-Low Phase Noise Oscillators

The phase noise (PN) of the traditional oscillator (i.e., class-B) with an ideal current source at an offset frequency $\Delta\omega$ from its fundamental frequency ω_0 could be expressed as

$$\mathcal{L}(\Delta\omega) = 10\log_{10}\left(\frac{KT}{2\,Q_t^2\,P_{DC}}\frac{1}{\alpha_I\,\alpha_V}\,(1+\gamma)\left(\frac{\omega_0}{\Delta\omega}\right)^2\right), \qquad (4.1)$$

where $\mathrm{Q_t}$ is the tank quality factor; α_I is the current efficiency, defined as the ratio of the fundamental current harmonic I_{ω_0} over the oscillator DC current $\mathrm{I_{DC}}$; and α_V is the voltage efficiency, defined as the ratio of the oscillation amplitude $\mathrm{V_{osc}}$ (single-ended) over the supply voltage $\mathrm{V_{DD}}$. The oscillator power consumption is

$$P_{DC} = \frac{V_{osc}^2}{\alpha_I \cdot \alpha_V \cdot R_{in}}, \tag{4.2}$$

where R_{in} is an equivalent input parallel resistance of the tank modeling its losses. Equation (4.1) clearly demonstrates a trade-off between power consumption and PN. To improve the oscillator PN, one must increase P_{DC} by scaling down R_{in}. This could be done by lowering the tank inductance while maintaining the optimal Q_t. For example, by keeping on reducing the inductance by half, R_{in} could theoretically decrease by half at the constant Q_t, which would improve phase noise by 3 dB with twice the power consumption at the same FoM.[1] However, at some point, the resistance of the tank's interconnections will start dominating the resonator losses and, consequently, the equivalent tank's Q will start decreasing. Hence, the PN-versus-power trade-off will no longer be beneficial since the FoM will drop dramatically due to the Q-factor degradation.

Coupling N oscillators is an alternative way of trading off the power for PN since it avoids scaling the inductance down to impractically small values. It can theoretically improve PN by a factor of N compared to a single oscillator [12, 13]. Unfortunately, the oscillator size increases linearly, i.e., $4\times$ larger area for just 6 dB of PN improvement.

In this chapter, we explain how to improve phase noise by utilizing two 1:n transformers that are connected back-to-back [8], as shown in Figure 4.1(b, c). The equivalent R_{in} and, thus, the oscillator PN are scaled down by a factor of $\sim(1 + n^2)$ without sacrificing tank's Q-factor. Hence, PN improvement can potentially be much better than with the coupled oscillators (e.g., Figure 4.1(a)) at the same die area. In addition, the C_2 and C_3 tuning capacitors, which are not directly connected to the primary of the first transformer, appear at the input of the transformer network via the scaling factor of n^2 and n^4 as can be realized from Figure 4.1(c). This impedance transformation results in a significant reduction in the required value of all the capacitors (i.e., $\sum_i C_i$), which reduces the routing parasitics (both inductive and capacitive), and improves the tuning range and PN of the oscillator. Even though by increasing the transformer's turns ratio the tank input impedance will be reduced, the transformer Q-factor will not stay at the optimum level and will start dropping at some point [14]. It turns out that the turns ratio of $n = 2$ can satisfy the aforementioned constraints altogether.

[1] FoM $= |\text{PN}| + 20\log_{10}(\omega_0/\Delta\omega) - 10\log_{10}(P_{DC}/1\text{mW})$.

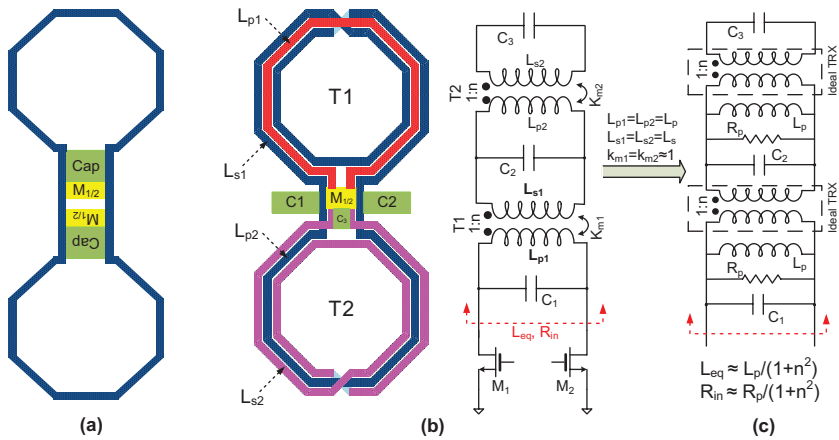

Figure 4.1 Phase noise reduction techniques without sacrificing tank's Q-factor: (a) coupled oscillators, (b) connecting two step-up transformers back-to-back, and (c) its equivalent circuit model.

To sustain the oscillation of this differential tank, two transistors shall be added. Figure 4.2 illustrates the *preliminary* schematic and waveforms. Unfortunately, as gathered from Figure 4.3, this structure suffers the same issues as the traditional class-B oscillator when the ideal current source is replaced with a tail bias transistor, M_T. The PN is ideally improved by 20 dB/dec through increasing the oscillation amplitude, provided the gm-devices $M_{1,2}$ operate in saturation over the entire period. However, the slope of PN improvement deviates from the ideal case when $M_{1,2}$ enter the triode region for a part of the oscillation period [15]. This problem is intensified especially when the oscillator operates at higher frequencies and larger I_{DC} (i.e., $\geq$10 mA) is needed to satisfy the stringent spectral purity of the GSM standard [16]. Actually, the combination of the parasitic drain capacitance of the large-size M_T with the entering the triode region by $M_{1,2}$, cyclically short-circuits the tank, thus degrading its equivalent Q-factor and oscillator PN [17].

Furthermore, the oscillation voltage should provide minimum V_{DSAT} across M_T throughout the entire period to keep it in saturation. Consequently, α_V becomes substantially less than 1, which translates to a significant PN penalty as clearly seen from (4.1). Larger M_T needs lower V_{DSAT}, which would increase α_V. However, the tail transistor's effective thermal noise will increase significantly for the same I_{DC} [18]. As a consequence, the contribution of M_T to the PN could be larger than that of gm-devices, which

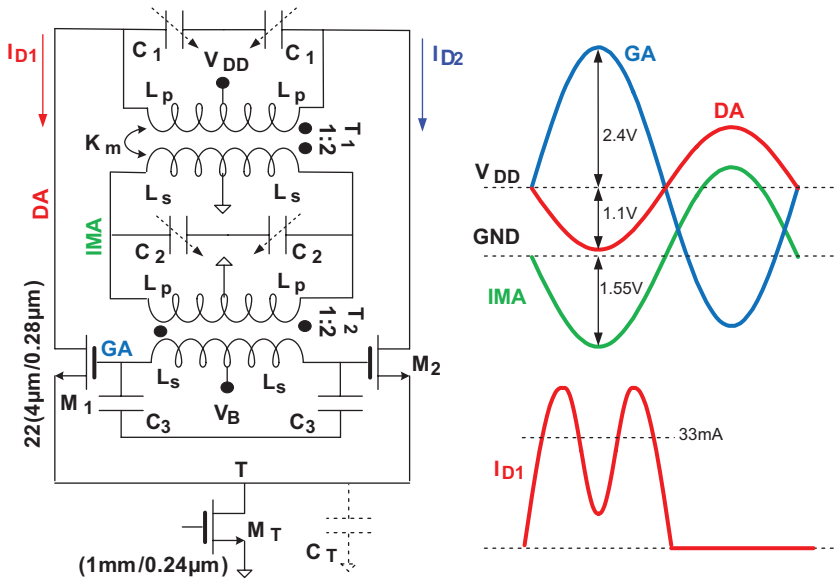

Figure 4.2 Preliminary oscillator schematic and its simulated voltage and estimated current waveforms at $f_0 = 8$ GHz, $V_{DD} = 1.2$ V, $I_{DC} = 33$ mA, $L_{eq} = 80$ pH, and $C_{eq} = 4.95$ pF.

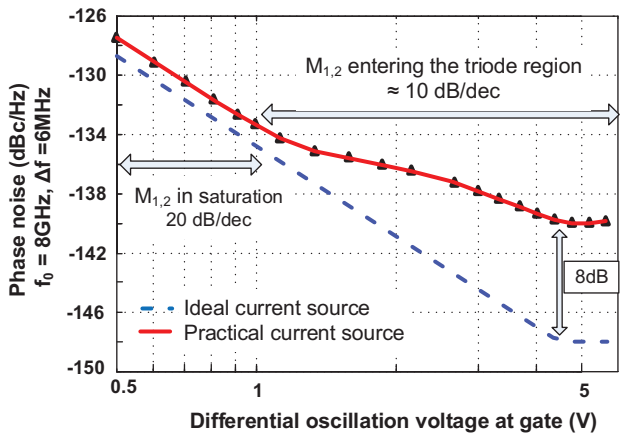

Figure 4.3 Simulated phase noise performance of the preliminary oscillator of Figure 4.2 versus gate differential oscillation voltage for the ideal and real current sources.

translates to a significant increase of the oscillator NF and thus its PN [16]. In addition, the M_T parasitic capacitance, C_T, will also increase with the side effect of a stronger tank loading. On the other hand, the combination

of the sinusoidal drain voltage, large C_T, and the entering of triode region by $M_{1,2}$ will result in a dimple in the squarish shape of active device drain current (see Figure 4.2) with a 10%–20% reduction in α_I and thus FoM of the oscillator [1, 16]. All the above reasons contribute to reducing the rate of PN improvement versus V_{osc} to about 10 dB/dec when $M_{1,2}$ enter the triode region for a part of the oscillation period. Hence, a huge 8-dB PN difference in Figure 4.3 is observed between the ideal and real operation of the oscillator. Consequently, the novel oscillator must not be sensitive to the excess gm-device noise in the triode intervals. It should also break the trade-off between α_V and NF.

4.3 Evolution Towards Class-F_2 Operation

Before introducing a new phase noise (PN) reduction technique, let us take a closer look at the harmonic component of the drain current I_D of the M_1 and M_2 gm-devices in Figure 4.2. Ideally, I_D is a square wave containing fundamental and odd harmonics. The odd harmonics through M_1 and M_2 are 180° mutually out-of-phase and appear as differential-mode (DM) input signals for the tank. The I_D also contains even harmonics due to the large oscillation voltage, non linearity of $M_{1,2}$, and large parasitic capacitance of M_T. However, the even harmonics through M_1 and M_2 are mutually in-phase with ±90° phase shift to their related odd harmonics, as shown in Figure 4.4. Consequently, these even harmonics appear as a common-mode (CM) input for the tank. The conventional tank input impedance has only one

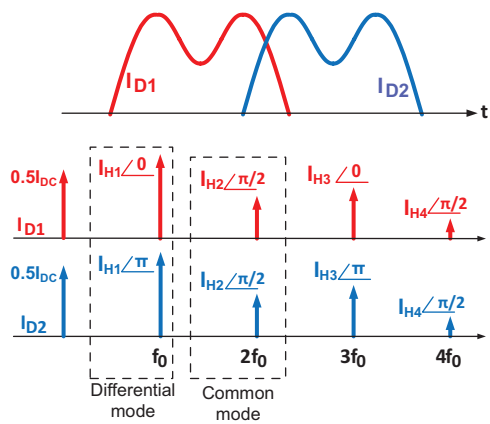

Figure 4.4 Drain current of $M_{1,2}$ devices of Figure 4.2 in time and frequency domains.

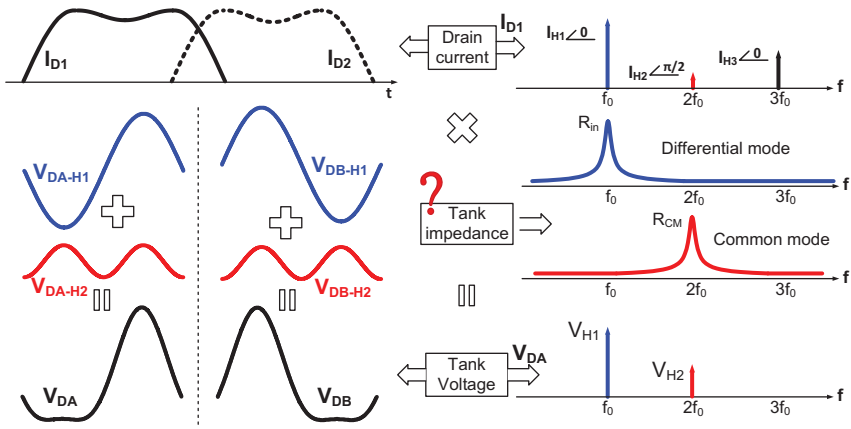

Figure 4.5 New oscillator's waveforms in time and frequency domains.

peak at the fundamental frequency ω_0. Therefore, the tank filters out the drain current harmonics and ultimately a sinusoidal voltage is seen across the tank. Now, suppose the tank offers an additional CM input impedance peak around the second harmonic (see Figure 4.5). Then, the second harmonic of I_D is multiplied by the tank's CM input impedance to produce a sinusoidal voltage at $2\omega_0$ that is in quadrature to the fundamental oscillation voltage produced by the tank's DM impedance at ω_0. The combination of both waveforms creates the desired oscillation voltage around the tank, as shown in Figure 4.5, thus justifying the class-F_2 designation.

$$V_{DA} = V_{DD} - V_{H1}\sin(\omega_0 t) - V_{H2}\sin\left(2\omega_0 t + \frac{\pi}{2}\right) \tag{4.3}$$

ζ_V is defined as the ratio of the second-to-first harmonic components of the oscillation voltage.

$$\zeta_V = \frac{V_{H2}}{V_{H1}} = \left(\frac{R_{CM}}{R_{in}}\right)\left(\frac{I_{H2}}{I_{H1}}\right), \tag{4.4}$$

where R_{in} and R_{CM} are, respectively, the tank DM and CM impedance magnitude at ω_0 and $2\omega_0$. Figure 4.6 illustrates the oscillation voltage and its related impulse sensitivity function (ISF) based on Equation (38) in [21] for different ζ_V values. Clearly, ζ_V should be 0.3 to have the widest flat span in the tank's oscillation voltage. The Γ^2_{rms} is 0.35 for $\zeta_V = 0.3$ compared to 0.5 for the traditional oscillator, which leads to a 1.5-dB PN and FoM improvements. Furthermore, ISF is negligible when the gm-devices work in the triode region

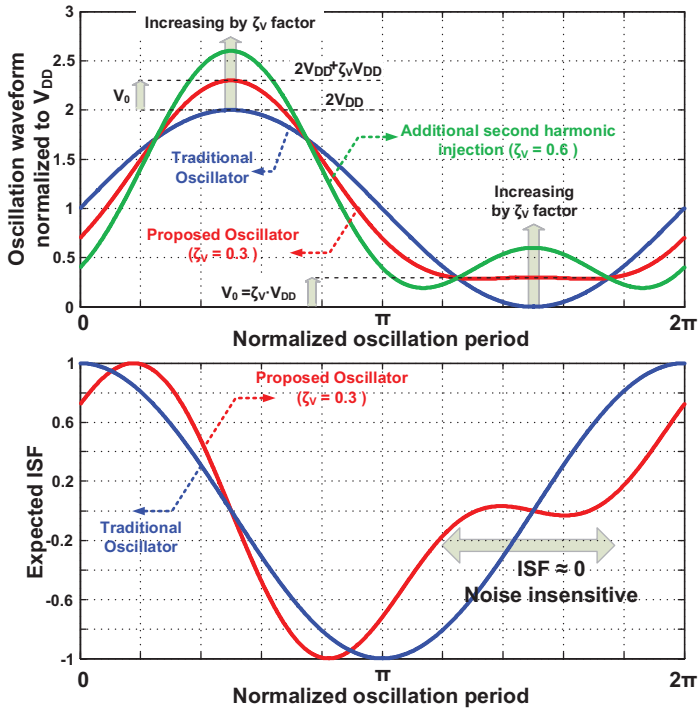

Figure 4.6 Effect of adding second harmonic in the oscillation voltage waveform (top) and its expected ISF based on Equation (38) in [21] (bottom).

and inject the most thermal noise into the tank. Consequently, the oscillator FoM improvement should be larger than that predicted by just the $\mathrm{ISF_{rms}}$ reduction. More benefits of the class-F_2 operation will be revealed in the following sections.

The argument related to Figure 4.5 suggests the creation of an additional CM input impedance peak at the second harmonic of main differential resonance. Incidentally, the introduced step-up 1:2 transformer acts differently to the CM and DM input signals. Figure 4.7(a) illustrates the induced current at the transformer's secondary when the primary winding is excited by a differential signal. All induced currents circulate in the same direction at the transformer's secondary to satisfy Lenz's Law. Consequently, the induced currents add constructively, which leads to a strong inter-winding coupling factor ($\mathrm{k_m} \geq 0.7$). However, when the transformer's primary is excited by a CM signal (Figure 4.7(b)), the induced currents at the right-hand and left-hand halves of the transformer's secondary winding circulate in opposite directions, thus

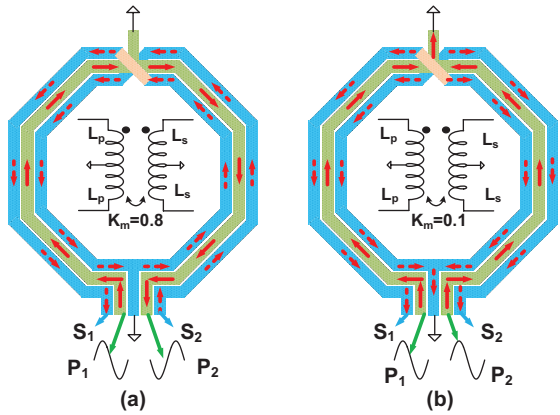

Figure 4.7 Transformer behavior in (a) differential-mode and (b) common-mode excitations.

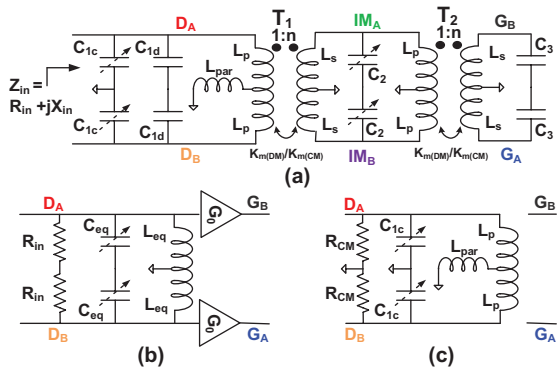

Figure 4.8 New transformer-based resonator: (a) schematic, (b) its simplified equivalent differential-mode circuit ($k_{m(DM)} \approx 1$), and (c) simplified tank schematic for common-mode input signals ($k_{m(CM)} \approx 0$).

largely canceling each other. The residual current results in a very small $k_m \leq 0.2$ for the CM excitation. Consequently, the concept of using two modes of a transformer for waveform shaping (proposed in [19] for a power amplifier) will be adopted here to realize the special tank input impedance of Figure 4.5. Note that an equivalent lumped-element model in [14, 20] cannot simultaneously cover both CM and DM types of behavior, and would produce wrong results. Hence, we suggest to utilize the transformer's S-parameters and PSS analysis to simulate the novel class-F_2 oscillator.

Figure 4.8 shows the newly invented tank of a class-F_2 oscillator. The C_{1d} and C_3 are intentionally chosen as fixed capacitors while the DM and

CM resonant frequencies are tuned by C_{1c} (fine) and C_2 (coarse). The DM main resonant frequency is

$$f_{1d} = \frac{1}{2\pi\sqrt{L_{eq}C_{eq}}} \approx \frac{1}{2\pi\sqrt{\left(\frac{L_p}{1+n^2}\right)(C_{1c} + C_{1d} + C_2 n^2 + C_3 n^4)}}. \quad (4.5)$$

The inductance reduction and capacitance multiplication factors of the dual-transformer tank are directly contained in (4.5). The CM input signal can neither see the second transformer nor C_2 and C_3 due to negligible $k_{m(CM)}$. In addition, differential capacitors also act as open circuit for the CM signals. Consequently, the tank's CM resonant frequency is

$$f_{1c} = \frac{1}{2\pi\sqrt{L_{cm}C_{1c}}} \approx \frac{1}{2\pi\sqrt{(L_p + 2L_{par})\,C_{1c}}}. \quad (4.6)$$

There is no tank impedance scaling for the CM excitation. Hence, the CM input impedance peak should be higher than the DM peak, as clearly seen from Figure 4.9 (top). To operate properly, CM-to-DM resonance ratio must be adjusted to 2:

$$\zeta_f = \frac{f_{1c}}{f_{1d}} = \sqrt{\frac{L_p}{L_p + 2L_{par}} \cdot \frac{C_{1c} + C_{1d} + C_2 n^2 + C_3 n^4}{C_{1c}\,(1+n^2)}} = 2. \quad (4.7)$$

As a consequence, the frequency tuning requires a bit different consideration than in the class-B oscillators. Both C_{1c} and C_2 must, at least at the coarse level, be changed simultaneously to satisfy (4.7) such that f_{1c} coincides with $2f_{1d}$. This adjustment is entirely a function of the ratio of the tuning capacitors, which is precise, thus making ζ_f largely independent from process, voltage, and temperature (PVT) variations.

Let us now consider the required accuracy of this ratio ζ_f. The transformer and switching capacitors are designed based on maximum Q-factor at the operating frequency f_{1d}. The tank Q-factor drops at least $3\times$ at $f_{1c} = 2f_{1d}$. Consequently, the tank CM impedance bandwidth is very wide, as seen in Figure 4.9. Therefore, the oscillator is less sensitive to the position of f_{1c} and thus the tuning capacitance ratio. A realistic 5% error in ζ_f has no significant adverse effects on the oscillator waveform and thus its PN.

The schematic and waveforms of the new oscillator are shown in Figures 4.10 and 4.11. Even though the second harmonic injection reduces the drain oscillation voltage by V_0 during the negative clipping interval,

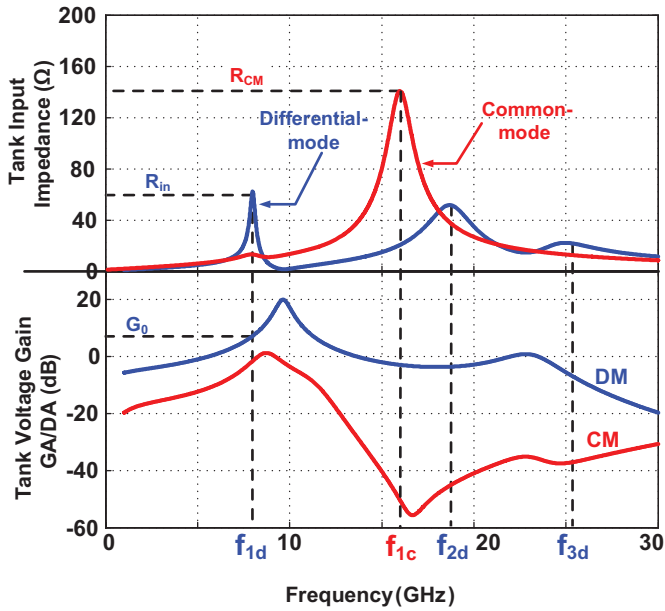

Figure 4.9 Simulated characteristics of the transformer-based tank of Figure 4.8: (top) magnitude of input impedance Z_{in}; (bottom) tank voltage gain between gate and drain of core devices.

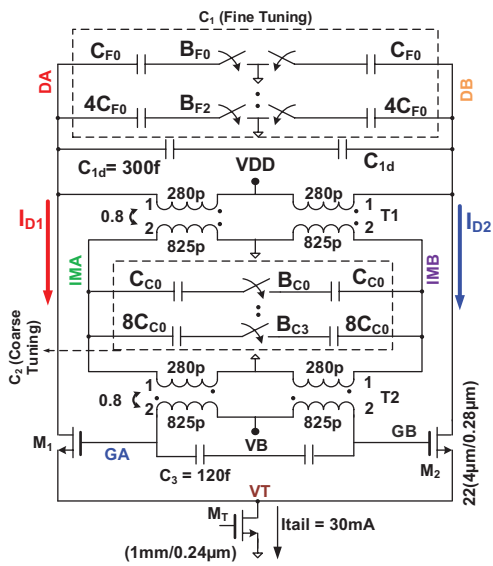

Figure 4.10 Transformer-based class-F_2 oscillator schematic.

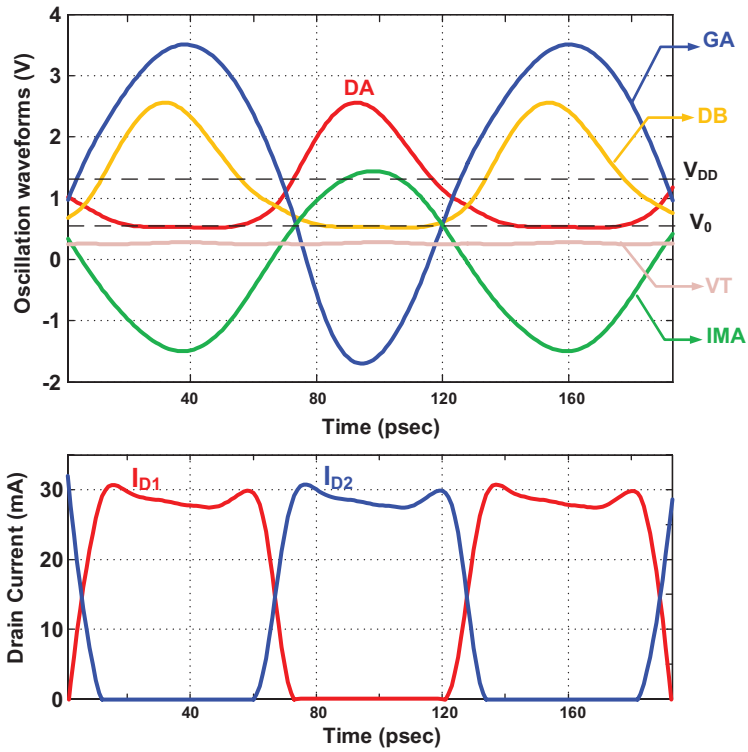

Figure 4.11 Simulated oscillation waveforms of the class-F_2 oscillator at $V_{DD} = 1.2$ V and $I_{DC} = 29$ mA: (top) oscillation voltage of different circuit nodes and (bottom) core transistors drain current.

it increases its positive peak by V_0 (see Figure 4.6(a)). It means the drain oscillation span is shifted from 0-to-2V_{DD} in the traditional oscillator to V_0-to-(2V_{DD} + V_0) in the class-F_2 operation. Hence, the larger current source voltage headroom and lower noise factor are achieved without compromising the oscillation amplitude. Furthermore, the V_0 headroom also reduces the dimple in the core-device drain current (compare Figures 4.2 and 4.11), which helps the class-F_2 current efficiency to be closer to the ideal value of $2/\pi$.

Figure 4.9 illustrates the tank CM/DM input impedance and passive voltage gain between the gate and drain of $M_{1,2}$ versus frequency. Unfortunately, the tank exhibits two other undesired DM resonant frequencies (f_{2d}, f_{3d}) due to imperfect k_m of the two transformers that create two leakage inductances [14]. Consequently, the circuit loop must guarantee the

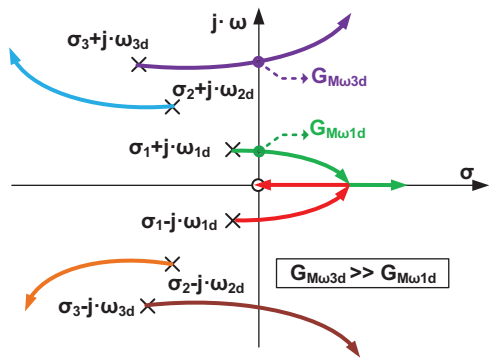

Figure 4.12 Root-locus plot of the class-F_2 oscillator.

oscillation only at the desired DM resonance, f_{1d}. Although CM demonstrates much larger input impedance peak, the two transformers effectively reject (attenuate by >40 dB) the CM signals. The root-locus plot in Figure 4.12 illustrates the DM pole movements toward zeros for different oscillator loop transconductance gains G_M. The first and third frequency conjugate pole pairs (ω_{1d}, ω_{3d}) move into the right-hand plane by increasing the absolute value of G_M, while the second conjugate pole ω_{2d} is pushed far away from the imaginary axis. This guarantees that the oscillation will not happen at ω_{2d}. Furthermore, it can be shown that ω_{3d} poles move to much higher frequencies with much lower input impedance peak and tank voltage gain if enough differential capacitance is located at T_1 primary windings. It justifies the existence of the non-switchable differential capacitor C_{1d}. Consequently, the loop gain will not be enough to satisfy the Barkhausen criterion for ω_{3d}.

4.4 Phase Noise Mechanism in Class-F_2 Oscillator

According to the linear time-variant (LTV) model [21], the phase noise of an oscillator at an offset frequency $\Delta\omega$ from its fundamental frequency ω_0 is expressed as

$$\mathcal{L}(\Delta\omega) = 10\log_{10}\left(\frac{\sum_i N_{L,i}}{2\, q_{max}^2\,(\Delta\omega)^2}\right), \tag{4.8}$$

where $q_{max} = C_{eq}{\cdot}V_{osc}$ is the maximum charge displacement across the tuning capacitors and $V_{osc} = \alpha_I{\cdot}R_{in}{\cdot}I_{DC}$ is the single-ended oscillation amplitude at the drain of gm-devices. The $N_{L,i}$ in (4.8) is the effective noise

power produced by $i\mathrm{th}$ device given by

$$N_{L,i} = \frac{1}{2\pi}\int_0^{2\pi} \Gamma_i^2(\omega_0 t)\,\overline{i_{n,i}^2(\omega_0 t)}d\,(\omega_0 t), \tag{4.9}$$

where $\overline{i_{n,i}^2}$ is the white noise current density of the $i\mathrm{th}$ noise source and Γ_i is its corresponding ISF function. Obtaining the ISF of various oscillator nodes is the first step in calculating the oscillator's PN. The ISF functions are simulated by injecting a 20 femto-coulomb charge (Δq) throughout the oscillation period and measuring the resulting time shifts, Δt_i.

$$\Gamma_i = \omega_0 \cdot \Delta t_i \cdot \frac{q_{max}}{\Delta q} \tag{4.10}$$

Figure 4.13(a) illustrates the ISF of various tank nodes. The soft clipping reduces by 30% the effect of losses on the oscillator PN due to single-ended switchable $\mathrm{C_{1c}}$[2] and $\mathrm{T_1}$ primary windings. However, ISF functions of the $\mathrm{T_1}$ secondary and $\mathrm{T_2}$ primary/secondary winding noise sources (including $\mathrm{C_2}$ and $\mathrm{C_3}$) are not improved due to the sinusoidal (i.e., conventional) waveforms at $\mathrm{IM_{A,B}}$ and $\mathrm{G_{A,B}}$ nodes. Figure 4.13(a) indicates that $\mathrm{G_{A,B}}$ are the most sensitive nodes. Hence, $\mathrm{C_3}$ is constructed as a fixed MoM capacitor and the transformer was designed with a goal of maximizing Q-factor of the secondary winding.

To calculate a closed-form PN equation, the oscillator model is simplified in Figure 4.14. The $\mathrm{G_{DS1,2}(t)}$ represent the channel conductance of $\mathrm{M_{1,2}}$. The $\mathrm{G_{M1,2}(t)}$ and $\mathrm{G_{MT}(t)}$ model the transconductance gain of $\mathrm{M_{1,2}}$ and $\mathrm{M_T}$, respectively. The original tank is pruned to a parallel $\mathrm{L_{eq}}$, $\mathrm{C_{eq}}$, $\mathrm{R_{in}}$ with noiseless voltage gain of $\mathrm{G_0}$ (see Figure 4.8(b)). The simplified tank's equivalent ISF can be roughly estimated by an average of the tank's contributing ISF functions of Figure 4.13(a) and is shown in Figure 4.13(b) as green curve. The effective noise power of the tank is illustrated in Figure 4.13(c) as green curve and its average power is approximated by

$$N_{Tank} = \frac{1}{\pi}\int_0^{2\pi} \frac{4KT}{R_{in}}\Gamma_{tank}^2(\omega_0 t)d(\omega_0 t) \approx 0.8\frac{KT}{R_{in}}. \tag{4.11}$$

Consequently, the soft clipping reduces $\mathrm{N_{Tank}}$ by 20% compared to the traditional oscillator.

[2]The single-ended switchable capacitor is used to adjust the CM resonant frequency. However, its Q-factor is almost half of that of the differential structure for the same $\mathrm{C_{max}/C_{min}}$. The soft clipping largely compensates the effect of additional losses due to its lower Γ_{rms} value.

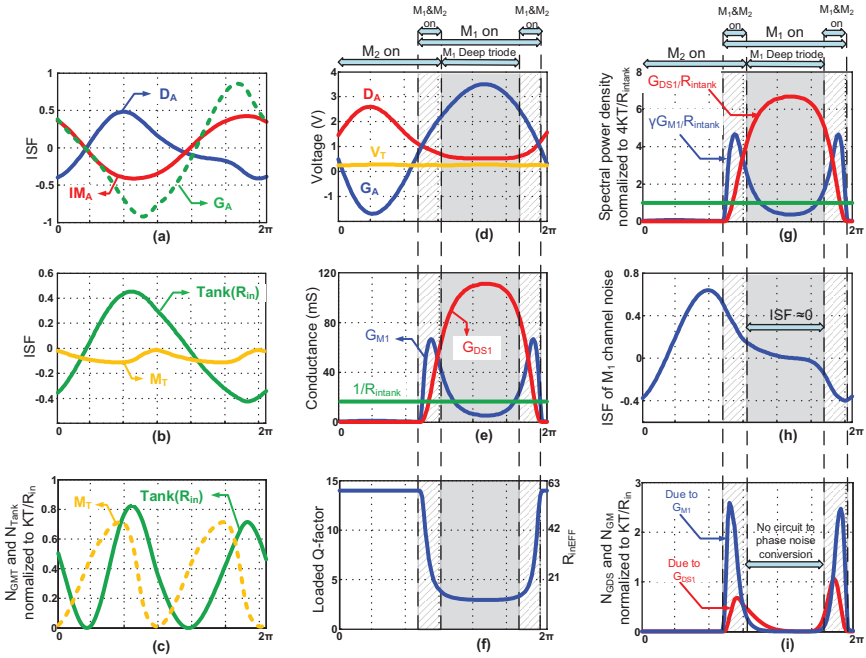

Figure 4.13 Mechanisms of circuit-to-phase-noise conversion across the oscillation period in the class-F_2 oscillator: (a) simulated ISF of different tank nodes, (b) equivalent ISF in the simplified oscillator schematic of Figure 4.14, (c) simulated effective power spectral density of the oscillator's noise sources normalized to $\mathrm{KT/R_{in}}$, (d) oscillation waveforms and operation region of $\mathrm{M_{1,2}}$, (e) transconductance and channel conductance of $\mathrm{M_1}$, (f) loaded Q-factor and effective parallel input resistance of the tank, (g) power spectral density of $\mathrm{M_1}$ noise sources normalized to $\mathrm{4KT/R_{in}}$, (h) simulated ISF function of $\mathrm{M_1}$ channel noise, and (i) simulated effective power spectral density of different noise sources of $\mathrm{M_1}$ normalized to $\mathrm{KT/R_{in}}$.

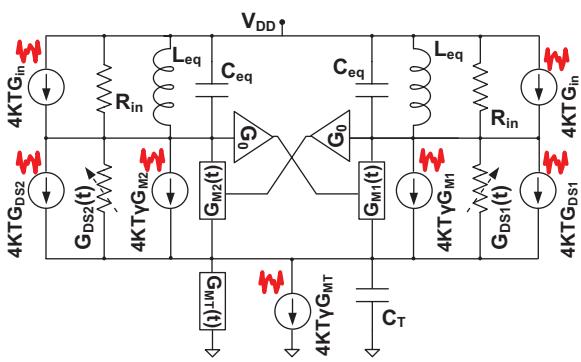

Figure 4.14 Simplified noise source model of the class-F_2 oscillator.

The effects of noise on the oscillator PN due to channel conductance (G_{DS}) and transconductance gain (G_M) of $M_{1,2}$ transistors are separately investigated. Figure 4.13(d) illustrates various operational regions of $M_{1,2}$ across the oscillation period. When $M_{1,2}$ are not turned off, they work mainly in the deep triode region where they exhibit a few ohms of channel resistance, as indicated in Figure 4.13(e). Consequently, the combination of the large parasitic capacitance of M_T with low channel resistance of $M_{1,2}$ in this deep triode region makes a low impedance path between the tank and ground. The literature interprets this as the tank loading event and defines implicit parameters such as *effective* tank Q-factor (Q_{eff}) and input parallel resistance (R_{ineff}) to justify the oscillator phase noise degradation due to this phenomenon. As shown in Figure 4.13(f), the tank Q_{eff} and R_{ineff} drop 4–5$\times$ when $M_{1,2}$ operate in the deep triode. These "effective" parameters merely indicate that more noise is injected then into the tank. However, they do not ordain how much of that circuit noise converts to phase noise, especially when the drain oscillation wave is not conventionally sinusoidal.

The proper approach should be based on the channel conductance noise power and its related ISF. If we had an ideal current source, $M_{1,2}$ noise would be injected to the tank only during the commutating time (hachure areas in Figure 4.13(e–g)). At the remaining part of oscillation period, one transistor is off and the other one is degenerated by the ideal current source and thus noiseless. However, the output impedance of a practical current source is low for such a high $I_{DC} = 30$ mA and $f_0 = 8$ GHz. Consequently, $M_{1,2}$ can inject significant amount of noise to the tank when they operate in deep triode region outside the commutating time (i.e., gray area in Figure 4.13(g)). Note that gm-devices generate $\sim$7$\times$ higher amount of noise compared to the tank loss in the gray area, which can potentially increase the phase noise of the oscillator. However, the ISF of channel noise of $M_{1,2}$ is very small in that time span as shown in Figure 4.13(h). Hence, the excessive transistor channel noise (or excessive loaded tank noise of the conventional approach) cannot convert to phase noise. Consequently, the effective noise power of the gm-device channel conductance is negligible, as illustrated in Figure 4.13(i), and its average power is approximated by

$$N_{GDS} = \frac{1}{\pi}\int_0^{2\pi} 4KTG_{DS1}(\omega_0 t)\cdot\Gamma_{M1}^2(\omega_0 t)\cdot d(\omega_0 t) \approx \frac{KT}{R_{in}}\cdot(0.25) \quad (4.12)$$

Note that N_{GDS} is at least 4$\times$ larger for the traditional oscillator, especially when a large α_V is needed [22].

Figure 4.13(e) shows M_1 transconductance gain G_{M1} across the oscillation period. To sustain the oscillation, the combination of the transformers' passive voltage gain (G_0) and effective negative transconductance of the gm-devices needs to overcome the tank and $M_{1,2}$ channel resistance losses. Consequently,

$$G_{M1EF} = \frac{1}{G_0} \cdot \left(\frac{1}{R_{in}} + G_{DS1EF} \right), \tag{4.13}$$

where G_{DS1EF} describes the effective value of the instantaneous conductance $G_{DS1}(t)$ of $M_{1,2}$ [22]. It can be shown that G_{DS1EF} could be as large as $1/R_{in}$ when the oscillator is biased near the voltage limited region [1]. Therefore, the effective noise due to G_M of core transistors can be calculated by

$$\begin{aligned} N_{GM} &= \frac{1}{\pi} \int_0^{2\pi} 4KT\gamma_{M1} G_{M1}(\omega_0 t) \cdot \Gamma_{M1}^2(\omega_0 t) \cdot d(\omega_0 t) \\ &\approx \frac{KT}{R_{in}} \frac{\gamma_{M1}}{G_0} \cdot (1 + R_{in} \cdot G_{DS1EF}) \approx \frac{KT}{R_{in}} \cdot \left(\frac{2\gamma_{M1}}{G_0} \right) \end{aligned} \tag{4.14}$$

Equation (4.14) indicates that the second harmonic injection (i.e., class-F_2 operation) demonstrates no benefit for N_{GM}, but the transformers' voltage gain still offers significant benefits.

To estimate the PN contribution of M_T, its transconductance should be calculated first.

$$G_{MT} = \frac{2I_{DC}}{V_{gs(M_T)} - V_{th}} \approx \frac{2I_{DC}}{V_T}, \tag{4.15}$$

where V_T is the overdrive voltage of M_T equal to the drain–source voltage. The clipping voltage level is

$$V_0 = V_{DD} \left[1 - \alpha_V \left(1 - \zeta_V \right) \right]. \tag{4.16}$$

By dedicating a half of V_0 headroom to M_T,

$$G_{MT} = \frac{4I_{DC}}{V_0} \approx \frac{4I_{DC}}{V_{DD} \left(1 - \alpha_V \left(1 - \zeta_V \right) \right)}. \tag{4.17}$$

By substituting I_{DC} with $V_{osc}/\left(\alpha_I R_{in}\right)$ in (4.17),

$$G_{MT} = \frac{4}{\left(1 - \alpha_V \left(1 - \zeta_V \right) \right) R_{in} \alpha_I} \left(\frac{V_{osc}}{V_{DD}} \right) = \frac{1}{R_{in}} \frac{4\alpha_V}{\left(1 - \alpha_V \left(1 - \zeta_V \right) \right) \alpha_I}. \tag{4.18}$$

As discussed earlier, $\alpha_{\rm I}$ and $\alpha_{\rm V}$ could be as large as 0.6 and 0.9 in this oscillator, and optimum $\zeta_{\rm V}$ is about 0.3. Hence, (4.18) is simplified to $G_{\rm MT} \approx 15/R_{\rm in}$. As revealed by Figure 4.13(b, orange), $\Gamma_{\rm MT,rms}$ is only 0.08 due to relatively large $V_{\rm T}$ of the class-F_2 operation. Consequently,

$$N_{MT} = \frac{1}{2\pi}\int_0^{2\pi} 4KT\gamma_{_{MT}} G_{MT}(\omega_0 t)\cdot\Gamma^2_{_{MT}}(\omega_0 t)\cdot d(\omega_0 t) \approx \frac{KT}{R_{in}}\cdot(0.4\gamma_{_{MT}})\,. \tag{4.19}$$

The contribution of $M_{\rm T}$ to the PN is less than that of the tank and is about 20% of the total. This share could easily be higher than 50% for the traditional oscillator at the same $\alpha_{\rm V}$ and $I_{\rm DC}$ as discussed in [16, 17]. Finally, the total oscillator effective noise power ($N_{\rm T}$) and noise factor ($NF_{\rm Total}$) are given by

$$N_T \approx \frac{KT}{R_{in}}\cdot NF_{Total}, \qquad NF_{Total} \approx \left(1.05 + \frac{2\gamma_{_{M1}}}{G_0} + 0.4\gamma_{_{MT}}\right). \tag{4.20}$$

Equation (4.20) indicates that the effective noise factor of the class-F_2 oscillator is very close to the ideal value of $(1+\gamma)$ despite the aforementioned practical issues. The phase noise can easily be calculated by replacing (4.20) in (4.8). The oscillator FoM normalizes the PN performance to ω_0 and $P_{\rm DC}$, yielding

$$FoM = -10\log_{10}\left(\frac{10^3\cdot KT}{2Q_t^2\alpha_I\alpha_V}\cdot NF_{Total}\right). \tag{4.21}$$

Table 4.1 verifies the solidity of the presented phase noise analysis by comparing the results of SpectreRF™ PSS, Pnoise simulations with the derived theoretical equations. The expressions estimate the oscillator PN and share of different noise sources with an acceptable accuracy.

It is also instructive to compare in Table 4.2 the benefits and drawbacks of the two flavors of class-F operation. Intuitively, the third-harmonic injection in class-F_3 (Chapter 3) demonstrates a pseudo-square waveform with smaller $ISF_{\rm rms}$ value and shorter commutating time. Consequently, it offers lower $NF_{\rm Tank}$ and $NF_{\rm GM}$. On the other hand, class-F_2 operation provides larger voltage overhead for the gm-devices and tail current transistor without sacrificing the oscillator α_V. Hence, it exhibits better $NF_{\rm MT}$, $NF_{\rm GDS}$, and $\alpha_{\rm V}$. As expected, the effective noise factor and FoM of both topologies turns out to be identical. However, this implementation of class-F_2 automatically scales down the tank input parallel resistance and thus offers lower PN at price of larger area and slightly lower Q-factor due to the interconnection of the two transformers.

Table 4.1 Comparison between the results of SpectreRF PSS, Pnoise simulation and theoretical equations at 8-GHz carrier for $V_{DD} = 1.2$ V, $R_{in} = 60\ \Omega$, $L_{eq} = 80$ pH, $\gamma_{MT} = 1.3$, and $\gamma_{M1,2} = 1$

	Theoretical Equations		SpectreRF Simulation	
	Value	Share	Value	Share
$\mathbf{N_{Tank}}$	$5.50 \cdot 10^{-23}$ V^2/Hz	31%	$4.71 \cdot 10^{-23}$ V^2/Hz	28.4%
$\mathbf{N_{M1,2} = N_{GDS} + N_{GMT}}$	$8.63 \cdot 10^{-23}$ V^2/Hz	48.8%	$8.78 \cdot 10^{-23}$ V^2/Hz	53%
$\mathbf{N_{MT}}$	$3.59 \cdot 10^{-23}$ V^2/Hz	20.2%	$3.08 \cdot 10^{-23}$ V^2/Hz	18.6%
$\mathbf{N_T = N_{Tank} + N_{M1,2} + N_{MT}}$	$17.72 \cdot 10^{-23}$ V^2/Hz	100%	$16.57 \cdot 10^{-23}$ V^2/Hz	100%
$\mathbf{q_{max}}$ **(coulumbs)**	$5.34 \cdot 10^{-12}$		$5.34 \cdot 10^{-12}$	
Phase noise @10MHz	−151 dBc/Hz		−151.33 dBc/Hz	

Table 4.2 Comparison between two flavors of class-F oscillator for the same carrier frequency = 8 GHz, $V_{DD} = 1.2$ V, tank Q-factor = 14, $\Delta f = 10$ MHz, and $R_P = 240\ \Omega$

	Expression	Class-F_3	Class-F_2
α_I	I_{ω_0}/I_{DC}	0.6	0.6
α_V	V_{osc}/V_{DD}	0.8	0.9 (✓)
$\mathbf{NF_{Tank}}$	$N_{Tank}/(KT/R_{in})$	0.7 (✓)	0.8
$\mathbf{NF_{GDS}}$	$N_{GDS}/(KT/R_{in})$	0.3	0.25 (✓)
$\mathbf{NF_{GM}}$	$N_{GM}/(KT/R_{in})$	$\approx 0.7\gamma_{M1}$ (✓)	$\approx \gamma_{M1}$
$\mathbf{NF_{GMT}}$	$N_{GMT}/(KT/R_{in})$	$\approx 0.5\gamma_{MT}$	$\approx 0.4\gamma_{MT}$ (✓)
$\mathbf{NF_{Total}}$		3.7dB (✓)	4.1dB
FoM	$\approx -10\log_{10}\left(\frac{KT}{2Q_t^2}\frac{}{\alpha_I\ \alpha_V}NF\right)$	192.9dB (✓)	192.9dB (✓)
$\mathbf{R_{in}}$		$\approx R_p = 240\Omega$	$\approx R_p/\left(1+n^2\right) = 60\Omega$ (✓)
$\mathbf{P_{DC}}$	$\left(\frac{V_{DD}^2}{R_{in}}\frac{\alpha_V}{\alpha_I}\right)$	8mW	36mW
Phase noise	$\approx 10\log_{10}\left(\frac{KT}{2Q_t^2\ P_{DC}}\frac{1}{\alpha_I\ \alpha_V}NF\left(\frac{\omega_0}{\Delta\omega}\right)^2\right)$	–144 dBc/Hz	–150.5 dBc/Hz (✓)

4.5 Experimental Results

This oscillator targets GSM-900 MHz and DSC-1800 MHz base-station PN requirements. Electromagnetic (EM) simulations reveal that the tank Q-factor would be slightly (i.e., ∼10%) better at 8 GHz as compared to 4 GHz for the

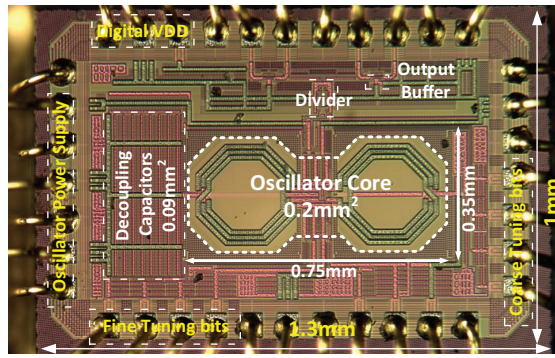

Figure 4.15 Die photograph of the class-F_2 oscillator.

same R_{in} and tuning range. However, the 1/f noise upconversion would be more severe at 8 GHz due to a larger share of the non linear C_{gs} of gm-devices to the total tank's capacitance. Furthermore, the output impedance of the current source is lower at higher frequencies, which would lead to higher PN penalty due to the tank loading. Consequently, there seems to be altogether no clear performance advantage of the 8 GHz over 4 GHz operation. Considering the fact that this oscillator has two transformers, the 8 GHz center frequency was chosen mainly to save die area.

The class-F_2 oscillator, whose schematic was shown in Figure 4.10, was realized in TSMC 1P7M 65 nm CMOS process technology. The die photograph is shown in Figure 4.15. The oscillator core die area is 0.2 mm^2. The differential transistors are thick-oxide devices of 22(4 μm/0.28 μm) dimension. However, the tail current source M_T is implemented as a standard 1 mm/0.24 μm thin-oxide ($t_{ox} = 2.6$ nm) device. Note that the thin-oxide device produces lower 1/f noise corner than the thick one at the same area [23]. The aluminum capping layer (1.45 μm), which is intended to cover bond pads, is strapped to the ultra-thick top copper layer (3.4 μm) to form the windings and improve the transformer's primary and secondary Q-factor to 14 and 20, respectively, at 8 GHz. The transformer's primary and secondary differential self-inductance is 560 and 1650 pH, respectively, with the DM and CM magnetic coupling factors of 0.8 and 0.15, respectively.

Four differential switched MOM capacitors $B_{C0}-B_{C3}$ with the resolution of 40 fF placed across T_1 secondary realize coarse tuning bits (C_2), while the fine control bits $B_{F0}-B_{F2}$ with LSB of 20 fF adjust ω_c to near $2\omega_{1d}$ to satisfy (4.7) and thus the class-F_2 operation. The effective C_{max}/C_{min} of the switched capacitor structures is determined by the strong trade-off between

the oscillator tuning range (TR) and tank Q-factor degradation due to the switch series resistance. The switched-capacitor's Q-factor is about 45 for 25% TR at 8 GHz. Furthermore, the interconnections of the two transformers also increase the tank losses by 10%, resulting in an average Q-factor of 14 for the entire tank.

The supply voltage connects to the center tap of T_1 primary along with a 100 pF on-chip decoupling capacitor. The center tap of T_2 secondary is connected to the bias voltage V_B, which is fixed at V_{DD} to minimize the number of supply domains and to guarantee safe oscillator start-up. The oscillator is very sensitive to noise at the $M_{1,2}$ gates (see Figure 4.13(a)). Fortunately, no DC current is drawn from V_B, so an RC filter of slow time constant is placed between V_{DD} and V_B to further reduce the bias voltage noise. Both T_1 secondary and T_2 primary winding center taps are connected to ground to avoid any floating nodes and make a return path for the negligible second-harmonic current to improve the waveform symmetry.

The measured and simulated PN at 4.35 GHz (after the on-chip ÷2 divider) at 1.3 V and 32 mA current consumption are shown in Figure 4.16.

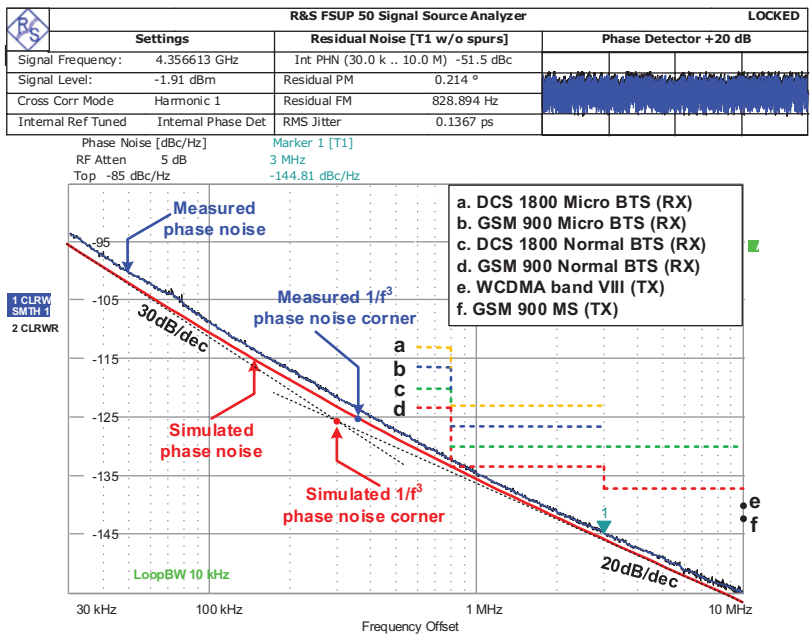

Figure 4.16 Measured (blue) and simulated (red) phase noise plots at 4.35 GHz, $V_{DD} = 1.3$ V and $P_{DC} = 41$ mW. Specifications (MS: mobile station, BTS: basestation) are normalized to the carrier frequency.

The PN of –145 dBc/Hz at 3 MHz offset lies on the 20 dB/dec region, which extrapolates to -174.7 dBc/Hz at 20 MHz offset (normalized to 915 MHz) and meets the GSM TX mobile station (MS) requirements with a very wide 13 dB margin. The GSM/DCS "micro" base-station (BTS) and DCS "normal" BTS specs are met with a few dB of margin. These PN numbers are the *best ever* published at low V_{DD} (i.e., $\leq$1.5 V). However, the toughest GSM base-station "normal" specifications at 800-to-900 kHz offset are within 1 dB of reach. The measured PN is just 1 dB higher than simulation in the 20-dB/dec region due to the power supply noise and additional tank loss caused by the routing of the tuning capacitors and dummy fill metals around the transformer.

The measured $1/f^3$ PN corner shows less than 100 kHz increase over the simulation and is $\sim$350 and $\sim$250 kHz at the highest and lowest side of the tuning range, respectively. This excellent $1/f^3$ performance is achieved, thanks to the following reasons: first, the 1/f noise of the tail current source can appear as a CM signal at T_1 primary and modulate the oscillation voltage. However, the T_1 transformer will effectively filter out this CM AM signal, thus preventing any AM-to-PM conversion at the C_2 switched capacitors and nonlinear C_{gs} of gm-devices. Second, the class-F_2 tank has two impedance peaks at the fundamental oscillation frequency and its second harmonic. Hence, the second harmonic of the drain current flows into a resistance of the tank instead of its capacitive part. It effectively reduces the 1/f noise upconversion to the $1/f^3$ phase noise due to Groszkowski phenomenon [24]; we will discuss this phenomenon intensively in Chapter 5. Third, the soft clipping effectively reduces the voltage variation of V_T, as shown in Figure 4.11. Intuitively, it could reduce the DC and even-order coefficients of ISF at this node and thus alleviate the 1/f noise conversion of the tail current transistor.

The PN noise beyond the 10-MHz offset is dominated by thermal noise floor from the divider and buffer set at –162 dBc/Hz. The oscillator has a 19% tuning range from 7.2 to 8.7 GHz. Figure 4.17 shows the phase noise and FoM of the oscillator at 3-MHz offset across the tuning range (after the $\div$2 divider). The average FoM is as high as 191 dBc/Hz and varies less than 2 dB. The oscillator also reveals a very low frequency pushing of 42 and 22 MHz/V at the highest and lowest frequencies, respectively.

Figure 4.18 shows the PN performance versus its current consumption. The circuit cannot satisfy Barkhausen oscillation criterion at $I_{DC} < 7$ mA. The oscillator phase noise is improved only by 10 dB/dec between 7 and 12 mA due to the drop in the oscillator current efficiency α_I and loading of the tank's Q-factor by the gm-devices entering the linear region. Note

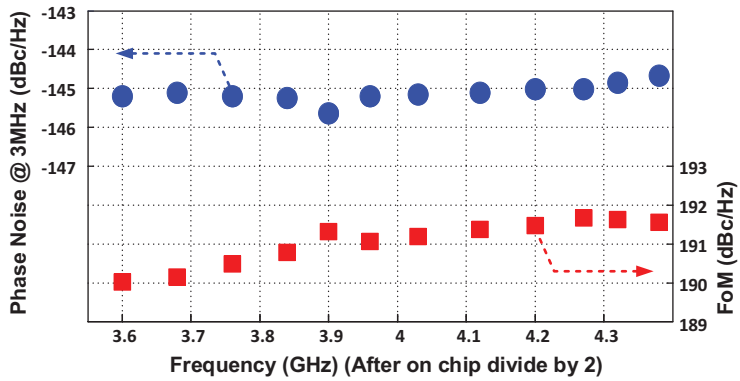

Figure 4.17 Measured phase noise and figure of merit (FoM) at 3 MHz offset versus carrier frequency.

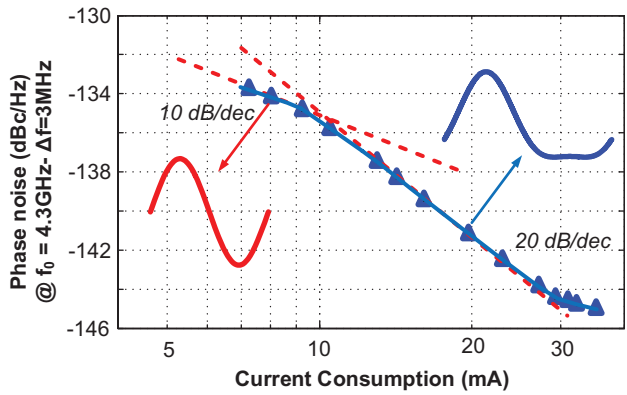

Figure 4.18 Measured phase noise at 3 MHz offset frequency from 4.3 GHz carrier versus the oscillator current consumption.

that even though the tank has an additional impedance at $2\omega_0$, the second harmonic of the drain current is negligible and, consequently, the drain oscillation resembles a sinusoid. However, by further increasing the drain current, the soft clipping phenomenon appears where the tank loading and tail transistor noise effects are reduced significantly due to the class-F_2 operation. Consequently, PN improves by almost 20 dB/dec, which demonstrates a few dB of improvement compared to the traditional class-B operation (compare Figures 4.3 and 4.18). Figure 4.18 also indicates that the circuit can sustain the oscillation even with $4\times$ lower I_{DC} and thus G_{MEF}, which translates into sufficient margin for the oscillator start-up over PVT variations.

Table 4.3 Comparison with relevant ultra-low phase noise oscillators

	This work	[13]	[27]	[1]	[17]	[25]	[26]
Technology	CMOS 65 nm	CMOS 65 nm	CMOS 65 nm	CMOS 65 nm	MOS 350 µm	CMOS 55 nm	BiCMOS 130 nm
Supply voltage (V)	1.3	2.15	1.5	1.25	2.5	1.5	3.3
Frequency (GHz)	4.35[1]	4.07	3.92[1]	3.7[1]	1.2	3.35[1]	1.56
Tuning range (%)	19	19	10.2	25	18	31.4	9.6
PN at 3 MHz (dBc/Hz)	−144.8	−146.7	−147.7	−142.2	−152	−142	−150.4
Norm. PN[2] (dBc/Hz)	−158.3	−159.6	−157.2	−154.3	−154.8	−153.3	−155
Power consumption (mW)	41.6	126.8	48	15	9.25	27	290
FoM (dB)	191.8[3]	188.3	190.1	192.2	195	189	180
FoM$_T$[4] (dB)	197.4	193.4	190.3	200.2	200.7	199	179.7
Transformers/ inductors count	2	2	2	1	2	1	1
Oscillator structure	Class-F_2	Dual core Class-C	Hard clipping	Class-F_3	Noise filtering	Class-B/ Class-C	Colpitts

[1] After on-chip ÷2 divider.
[2] At 3-MHz offset frequency normalized to 915-MHz carrier.
[3] FoM drops to 191.5 dB by considering the divider power consumption of 2.6 mW.
[4] $\text{FOM}_\text{T} = |\text{PN}| + 20\log_{10}((f_0/\Delta f)\ (\text{TR}/10)) - 10\log_{10}(P_{DC}/1\text{mW})$.

Table 4.3 summarizes the performance of the class-F_2 oscillator and compares it with the best spectral purity relevant oscillators. Note that this oscillator demonstrates the best PN with the highest power efficiency at a relatively low supply voltage. Only the dual-core class-C oscillator [13] offers better PN performance but at the price of 1.65× larger V_{DD}, 3× higher power consumption, and 3 dB lower FoM or power efficiency.

4.6 Conclusion

In this chapter, we have presented and analyzed a class-F_2 oscillator where an auxiliary impedance peak is introduced around the second harmonic of

the oscillating waveform. The second harmonic of the active device current converts into voltage and, together with the fundamental component, creates a soft clipped oscillation waveform. The class-F_2 operation offers enough headroom for the low noise operation of the tail current transistor without compromising the oscillator current and voltage efficiencies. Furthermore, the special ISF of the soft clipping waveform reduces significantly the circuit-to-phase-noise conversion. The additional resonant frequency is realized by exploiting a different transformer behavior in common-mode and differential-mode excitations. In addition, the tank input impedance is also scaled down without sacrificing its Q-factor. Consequently, this structure is able to push the phase noise much lower than practically possible with the traditional LC oscillators while satisfying long-term reliability requirements.

References

[1] M. Babaie and R. B. Staszewski, "A class-F CMOS Oscillator," *IEEE J. Solid-State Circuits*, vol. 48, no. 12, pp. 3120–3133, Dec. 2013.

[2] R. B. Staszewski and P. T. Balsara, *All-Digital Frequency Synthesizer in Deep-Submicron CMOS. Wiley*, 2006. Available: http://books.google.nl/books?id=2VHFD-7LgAwC.

[3] C. Weltin-Wu, G. Zhao, and I. Galton, "A 3.5 GHz digital fractional-N PLL frequency synthesizer based on ring oscillator frequency-to-digital conversion," *IEEE J. Solid-State Circuits*, vol. 50, no. 12, pp. 2988–3002, Dec. 2015.

[4] L. Vercesi, L. Fanori, F. D. Bernardinis, A. Liscidini, and R. Castello, "A dither-less all digital PLL for cellular transmitters," *IEEE J. Solid-State Circuits*, vol. 47, no. 8, pp. 1908–1920, Aug. 2012.

[5] K. Takinami, R. Strandberg, P. C. P. Liang, G. L. G. de Mercey, T. Wong, and M. Hassibi, "A rotary-traveling-wave-oscillator-based alldigital PLL with a 32-phase embedded phase-to-digital converter in 65 nm CMOS," *IEEE International Solid-State Circuits Conference Digest of Technical Papers (ISSCC)*, 2011, pp. 100–101.

[6] C. Hsu, M. Z. Straayer, and M. H. Perrott, "3.6 GHz digital $\Delta\Sigma$ fractional-N frequency synthesizer with a noiseshaping time-to-digital converter and quantization noise cancellation," *IEEE J. Solid-State Circuits*, vol. 43, no. 12, pp. 2776–2786, Dec. 2008.

[7] H. H. Chang, P.-Y. Wang, J.-H. Zhan, and H. Bing-Yu, "A fractional spur-free ADPLL with loop-gain calibration and phase-noise cancellation for GSM/GPRS/EDGE," *IEEE International Solid-State*

Circuits Conference Digest of Technical Papers (ISSCC), 2008, pp. 200–201.

[8] M. Babaie, A. Visweswaran, Z. He, and R. B. Staszewski, "Ultra-low phase noise 7.2–8.7 GHz clip-and-restore oscillator with 191 dBc/Hz FoM," *Proceedings of IEEE Radio Frequency Integrated Circuits (RFIC) Symposium*, 2013, pp. 43–46.

[9] M. Babaie and R. B. Staszewski, "An ultra-low phase noise class-F_2 CMOS oscillator with 191 dBc/Hz FOM and long term reliability," *IEEE J. Solid-State Circuits*, vol. 50, no. 3, pp. 679–692, Mar. 2015.

[10] R. B. Staszewski, M. Babaie, and Z. He, "Oscillator," *US Patent 9,337,847*, issued 10 May 2016.

[11] M. Babaie and R. B. Staszewski, "An ultra-low phase noise class-F_2 CMOS oscillator with 191 dBc/Hz FOM and long term reliability," *IEEE J. Solid-State Circuits*, vol. 50, no. 3, pp. 679–692, Mar. 2015.

[12] L. Romano, A. Bonfanti, S. Levantino, C. Samori, and A. L. Lacaita, "5-GHz oscillator array with reduced flicker up-conversion in 0.13-μm CMOS," *IEEE J. Solid-State Circuits*, vol. 41, no. 11, pp. 2457–2467, Nov. 2006.

[13] M. Tohidian, S. Mehr, and R. B. Staszewski, "Dual-core high-swing class-C oscillator with ultra-low phase noise," *Proceedings of IEEE Radio Frequency Integrated Circuits (RFIC) Symposium*, 2013, pp. 243–246.

[14] J. R. Long, "Monolithic transformers for silicon RF IC design," *IEEE J. Solid-State Circuits*, vol. 35, no. 9, pp. 1368–1382, Sept. 2000.

[15] A. Mazzanti and P. Andreani, "Class-C harmonic CMOS VCOs, with a general result on phase noise," *IEEE J. Solid-State Circuits*, vol. 43, no. 12, pp. 2716–2729, Dec. 2008.

[16] L. Fanori and P. Andreani, "Highly efficient class-C CMOS VCOs, including a comparison with class-B VCOs," *IEEE J. Solid-State Circuits*, vol. 48, no. 7, pp. 1730–1740, Jul. 2013.

[17] E. Hegazi, H. Sjoland, and A. A. Abidi, "A filtering technique to lower LC oscillator phase noise," *IEEE J. Solid-State Circuits*, vol. 36, no. 12, pp. 1921–1930, Dec. 2001.

[18] P. Andreani, X. Wang, L. Vandi, and A. Fard, "A study of phase noise in Colpitts and LC-tank CMOS oscillators," *IEEE J. Solid-State Circuits*, vol. 40, no. 5, pp. 1107–1118, May 2005.

[19] J. Chen, L. Ye, D. Titz, F. Gianesello, R. Pilard, A. Cathelin, F. Ferrero, C. Luxey, and A. Niknejad, "A digitally modulated mm-Wave cartesian beamforming transmitter with quadrature spatial combining,"

IEEE International Solid-State Circuits Conference Digest of Technical Papers (ISSCC), 2013, pp. 232–233.

[20] A. M. Niknejad and R. G. Meyer, "Analysis, design, and optimization of spiral inductors and transformers for Si RF ICs," *IEEE J. Solid-State Circuits*, vol. 33, no. 10, pp. 1470–1481, Oct. 1998.

[21] A. Hajimiri and T. H. Lee, "A general theory of phase noise in electrical oscillators," *IEEE J. Solid-State Circuits*, vol. 33, no. 2, pp. 179–194, Feb. 1998.

[22] D. Murphy, J. J. Rael, and A. A. Abidi, "Phase noise in LC oscillators: A phasor-based analysis of a general result and of loaded Q," *IEEE Transactions on Circuits and Systems I, Reg. Papers*, vol. 57, no. 6, pp. 1187–1203, Jun. 2010.

[23] C.-H. Jan, M. Agostinelli, H. Deshpande, M. El-Tanani, W. Hafez, U. Jalan, L. Janbay, M. Kang, H. Lakdawala, J. Lin, Y.-L. Lu, S. Mudanai, J. Park, A. Rahman, J. Rizk, W.-K. Shin, K. Soumyanath, H. Tashiro, C. Tsai, P. Vandervoorn, J.-Y. Yeh, and P. Bai, "RF CMOS Technology Scaling in High-k/Metal Gate Era for RF SoC (Systemon-Chip) Applications," *IEEE International Electron Devices Meeting (IEDM)*, 2010, pp. 604–607.

[24] J. Rael and A. Abidi, "Physical processes of phase noise in differential LC oscillators" *Proceedings of IEEE Custom Integrated Circuits Conference (CICC)*, 2000, pages: 569–572.

[25] L. Fanori, A. Liscidini, and P. Andreani, "A 6.7-to-9.2 GHz 55 nm CMOS hybrid class-B/class-C cellular TX VCO," in *IEEE International Solid-State Circuits Conference Digest of Technical Papers (ISSCC)*, 2012, pp. 354–355.

[26] J. Steinkamp, F. Henkel, P. Waldow, O. Pettersson, C. Hedenas, and B. Medin, "A Colpitts oscillator design for a GSM base station synthesizer," *Proceedings of IEEE Radio Frequency Integrated Circuits (RFIC) Symposium*, 2004, pp. 405–408.

[27] A. Visweswaran, R. B. Staszewski, and J. R. Long, "A low phase noise oscillator principled on transformer-coupled hard limiting," *IEEE J. Solid-State Circuits*, vol. 49, no. 2, pp. 300–311, Feb. 2014.